

# Collinear Laser Spectroscopy of Helium-like $^{11}\text{B}^{3+}$

Konstantin Mohr <sup>1,2,\*</sup>, Axel Buß <sup>3,†</sup>, Zoran Andelkovic <sup>4</sup>, Volker Hannen <sup>3</sup>, Max Horst <sup>1,2</sup>, Phillip Imgram <sup>1</sup>, Kristian König <sup>1</sup>, Bernhard Maaß <sup>1,5</sup>, Wilfried Nörtershäuser <sup>1,2</sup>, Simon Rausch <sup>1,2</sup>, Rodolfo Sánchez <sup>4</sup> and Christian Weinheimer <sup>3</sup>

<sup>1</sup> Institut für Kernphysik, Technische Universität Darmstadt, 64289 Darmstadt, Germany

<sup>2</sup> Helmholtz Forschungsakademie Hessen für FAIR HFHF, Campus Darmstadt, 64289 Darmstadt, Germany

<sup>3</sup> Institut für Kernphysik, Westfälische Wilhelms-Universität Münster, 48149 Münster, Germany

<sup>4</sup> GSI Helmholtzzentrum für Schwerionenforschung GmbH, 64291 Darmstadt, Germany

<sup>5</sup> Argonne National Laboratory, Lemont, IL 60439, USA

\* Correspondence: k.mohr@gsi.de

† These authors contributed equally to this work.

**Abstract:** Collinear laser spectroscopy in the  $1s2s\ ^3S_1 \rightarrow 1s2p\ ^3P_{0,2}$  transitions of helium-like  $^{11}\text{B}^{3+}$  was performed using the HITRAP beamline at the GSI Helmholtz Centre. The ions were produced in an electron beam ion source, extracted, and accelerated to a beam energy of 4 keV/q. Results agree with previous measurements within uncertainty. Thus, it was demonstrated that the metastable state in He-like ions is sufficiently populated to carry out collinear laser spectroscopy. The measurement is a pilot experiment for a series of measurements that will be performed at a dedicated collinear laser spectroscopy setup at TU Darmstadt with light helium-like ions.

**Keywords:** helium-like ions; boron; fine-structure splitting; collinear laser spectroscopy



**Citation:** Mohr, K.; Buß, A.; Andelkovic, Z.; Hannen, V.; Horst, M.; Imgram, P.; König, K.; Maaß, B.; Nörtershäuser, W.; Rausch, S.; et al. Collinear Laser Spectroscopy of Helium-like  $^{11}\text{B}^{3+}$ . *Atoms* **2023**, *11*, 11. <https://doi.org/10.3390/atoms11010011>

Academic Editors: Izumi Murakami, Daiji Kato, Hiroyuki A. Sakaue and Hajime Tanuma

Received: 31 October 2022

Revised: 22 December 2022

Accepted: 28 December 2022

Published: 11 January 2023



**Copyright:** © 2023 by the authors. Licensee MDPI, Basel, Switzerland. This article is an open access article distributed under the terms and conditions of the Creative Commons Attribution (CC BY) license (<https://creativecommons.org/licenses/by/4.0/>).

## 1. Introduction

The mean-square (ms) nuclear charge radius is a fundamental property of a nucleus. Changes of this observable along an isotopic chain can precisely be determined by laser spectroscopy [1,2]. The isotope shift  $\delta\nu^{AA'}$  in an electronic transition, i.e., the frequency difference between two isotopes with mass numbers  $A$  and  $A'$ ,

$$\delta\nu^{AA'} = \nu^{A'} - \nu^A = K_{\text{MS}} \frac{M_{A'} - M_A}{M_{A'} M_A} + F \delta\langle r_c^2 \rangle^{AA'}, \quad (1)$$

is caused by the change of the center-of-mass motion of the nucleus (mass-shift, MS, first term) and the potential difference for an electron at the nuclear site (field-shift, second term) caused by different nuclear charge radii  $\delta\langle r_c^2 \rangle^{AA'}$  of the two isotopes. The mass-shift factor  $K_{\text{MS}}$  and the field-shift factor  $F$  have to be empirically determined or calculated by atomic structure calculations. When referring to the ms radius of a reference isotope known from other sources—usually electron scattering or muonic X-ray spectroscopy—the total charge radius of an isotope can be extracted as well:

$$R_c(A) = \sqrt{R_{\text{ref}}^2 + \delta\langle r_c^2 \rangle^{A_{\text{ref}}, A}}. \quad (2)$$

This method has been applied across the nuclear chart for many stable and radioactive isotopes alike (see, e.g., [2]). For very light isotopes, mass-shift calculations and the determination of the field-shift have to be performed with very high accuracy, since the field-shift contribution is roughly four orders of magnitude smaller than the mass-shift. The interest in this region of the nuclear chart is primarily driven by the existence of so-called halo nuclei, i.e., nuclei that consist of a compact core of standard nuclear matter density and a far-reaching tail of dilute nuclear matter. A review of these measurements and the

theory is provided in [3]. Nowadays, nonrelativistic QED (NR-QED) calculations are even able to accurately provide mass-shifts in five-electron systems, as has been demonstrated for spectroscopy of stable boron isotopes [4]. The boron chain is different from the chains of He, Li, and Be, insofar that an accurate reference radius for the stable isotopes is currently not available. Elastic electron scattering reports relative uncertainties of the order of 5% [5], and even the model-dependent result of the muonic atom spectroscopy is still afflicted with a 2% uncertainty [6]. This is particularly disadvantageous for the determination of the charge radius of the proton-halo candidate  ${}^8\text{B}$  [7] since its charge radius has to be compared to the charge radius of  ${}^7\text{Be}$  in order to determine the size of the proton halo. Thus, its physics discussion will be fully afflicted with the uncertainty of the reference radius. While—to our knowledge—no electron scattering experiment is currently planned on boron, a collaboration has formed to improve the charge radii of light elements by muonic atom X-ray spectrometry using cryogenic microcalorimeters [8].

In principle, the nuclear size is directly imprinted in the atomic transition energy. If the level energies  $E_{\text{pl}}(i, f)$  of the initial (i) and final (f) level in an atomic system can be calculated accurately, assuming a finite mass but point-like (pl) nucleus, the ms charge radius can be determined from the measured transition frequency  $\nu_{\text{exp}}$  according to

$$R_c^2 = \frac{h\nu_{\text{exp}} - (E_{\text{pl}}(f) - E_{\text{pl}}(i))}{F} = \frac{h\nu_{\text{exp}} - h\nu_{\text{pl}}}{F}. \quad (3)$$

The field-shift factor  $F = Z/6\epsilon_0(|\psi_f(0)|^2 - |\psi_i(0)|^2)$  in lowest order, is dominated by the difference in the probability densities of the electron wavefunction at the nuclear site.

This approach has, thus far, been used exclusively for hydrogen-like systems: atomic hydrogen [9–11], muonic hydrogen  $\mu\text{H}$  [12], muonic deuterium  $\mu\text{D}$  [13], and muonic helium  $\mu\text{He}^+$  [14]. The measurements on hydrogen and muonic hydrogen constituted the so-called proton-radius puzzle. For a recent review on this topic, see [15]. Already for the two-electron system, the uncertainties of the nuclear level energies are larger than the nuclear finite size effect in these light systems, but substantial progress has been reported in recent years in the NR-QED treatment of helium and helium-like systems, as reported in [16–18].

Since the ground state in He-like systems is not accessible by conventional laser systems, only the metastable  $1s2s\,{}^3\text{S}_1$  can serve as initial state from which dipole allowed (E1) transitions to the  $1s2p\,{}^3\text{P}_1$  are laser accessible. However, since the lifetime of the  $2\,{}^3\text{S}_1$  state decreases rapidly with the atomic number from roughly 7900 s in He to 21 ms in helium-like carbon, a fast measurement technique is required. Collinear laser spectroscopy [19] has been used for many decades and has been proven to provide very accurate measurements [20,21], even on very short-lived isotopes [22]. A program to study the  $2\,{}^3\text{S}_1 \rightarrow 2\,{}^3\text{P}_J$  transitions in light He-like systems has therefore been initiated at the Collinear Apparatus for Laser Spectroscopy and Applied Physics (COALA) at TU Darmstadt [23], where it is foreseen to extract He-like ions from an electron beam ion source (EBIS) and to study them after acceleration to a few keV beam energy. Here, we report on a pilot experiment to explore the sufficient population of the metastable  $2\,{}^3\text{S}_1$  in  ${}^{11}\text{B}^{3+}$ , the resulting lineshape in fluorescence detection, and the achievable accuracy. Boron was chosen because of its interest for the determination of the nuclear charge radius of  ${}^8\text{B}$  and the fact that the transition frequencies are already comparably well known from a previous collinear laser spectroscopy experiment by Dinnéen et al. [24], which limits the range to search for the resonance line.

## 2. Experimental Setup

Measurements were carried out at the GSI Helmholtz Center in Darmstadt using the SPARC EBIT [25], a compact room-temperature Dresden-type EBIT, and the HITRAP beamline [26] to transport the ions to the SPECTRAP experiment [27]. A schematic drawing of the HITRAP low-energy beamline and its connection to the vertical SPECTRAP beamline is shown in Figure 1.

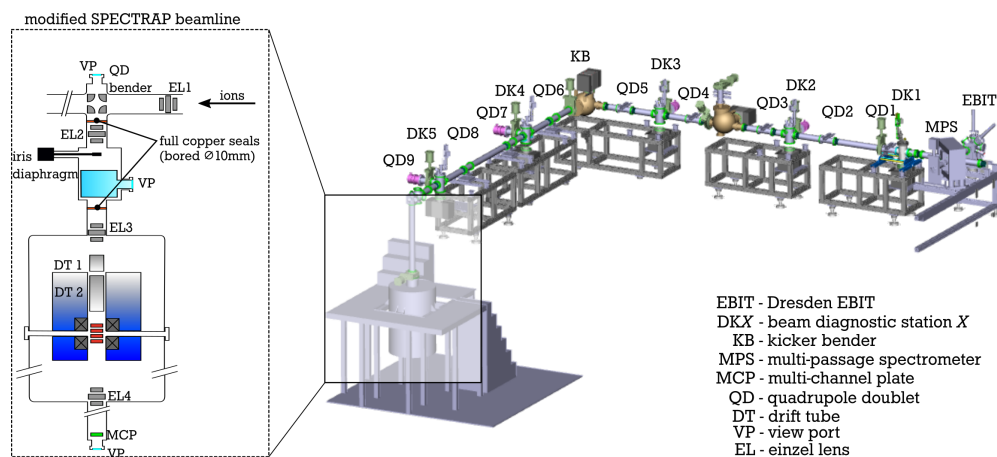


**Figure 1.** Schematic drawing of the HITRAP low-energy beamline (right) and a more detailed figure of the modified SPECTRAP beamline (left).

He-like  $^{11}\text{B}^{3+}$  was produced inside the SPARC-EBIT using the metal-ion from volatile compounds (MIVOC) method. The volume above a small amount of liquid trimethylborate (TMB) is evacuated until a substantial fraction of the liquid is evaporated and the atmosphere above the remaining substance is dominated by TMB molecules. This vapor is then fed into the center of the EBIT via a feedback-loop controlled needle-valve that stabilizes the pressure inside the EBIT during operation to  $2 \cdot 10^{-9}$  mbar (standby pressure  $\approx 10^{-10}$  mbar). Once the molecule is broken up by the impact of the dense electron beam, its constituents are ionized subsequently. The final distribution of charge states depends on the confinement time, the electron current, and the depth of the axial potential well.

The composition of the extracted ion bunch was analyzed using a combined  $m/q$  separation in the magnetic  $90^\circ$  multipassage spectrometer (MPS) of the HITRAP low-energy beamline [26] and a time-of-flight determination using the arrival signal of the ions at the multichannel plate (MCP) below the SPECTRAP magnet [27]. Optimization of the ion number in the correct charge state, taking the duty cycle of the spectroscopy experiment into account, led to an operation at an electron current of 18–20 mA and a charge breeding (confinement) time of 12 ms. The beam energy is determined by the potential of the central drift tube in the EBIT, which was set to 4 kV. This is the maximum energy at which the  $\text{B}^{3+}$  ions can still be transported through the  $90^\circ$  quadrupole bender, which connects the HITRAP low-energy beamline and the SPECTRAP setup.

Since the SPECTRAP experiment was originally only foreseen for high-precision laser spectroscopy in a penning-trap, it needed to be equipped with an optical detection region (ODR) dedicated for collinear laser spectroscopy [28]. The ODR implemented at SPECTRAP was the prototype of the optical detection region for collinear laser spectroscopy at CRYRING@ESR. It was mounted in a vertical direction above the SPECTRAP magnet, as indicated in the left panel of Figure 1 and in more detail in Figure 2, where picture of the mounted setup is also shown in the right panel. Inside the vacuum, an elliptical mirror system made of aluminum plates (MIRO 3 by Alanod) is held by a frame made of PEEK and insulated against the conducting walls of the vacuum chamber. The more distant focal axes of the mirror system are aligned with the laser and ion beam axis. The second focal axis is close to the quartz window, on which a photomultiplier tube (PMT) of type 9235QB from ET Enterprise Ltd. with a dark count rate of  $\sim 150 \text{ s}^{-1}$  is mounted outside

the vacuum. Due to the elliptical design, fluorescent light originating from the excited ions is accumulated more efficiently than scattered light originating from different locations along the beam line. Apertures of 20 mm diameter in the lower and upper back planes of the ODR provide sufficient space to overlap the laser and ion beam inside the ODR. Electrostatic quadrupoles in front of the 90°-bender and an einzel lens after the bender were used to optimize the ion beam shape inside the interaction region. Full copper seals with a central bore of 10 mm diameter below and above the interaction region ensured a proper alignment of the ion and the laser beams. The laser position was additionally monitored by a camera above the exit window and could be optimized using a movable iris diaphragm.

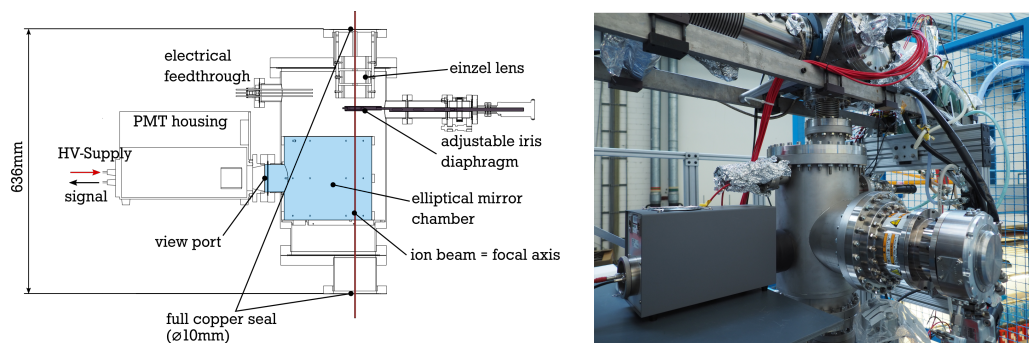


**Figure 2.** Schematic drawing of the optical detection region (left) and photo of the assembled vacuum system (right).

The pulsed extraction from the EBIT allowed us to limit the photon detection to intervals of ion passages through the ODR and, thereby, to suppress background from scattered laser light. Each registered photon is recorded with a time stamp of its appearance to be able to choose time intervals of interests in the offline analysis. Details of the data acquisition system (“TILDA”) can be found in [29,30].

To address the fine-structure transitions  $2^3S_1 \rightarrow 2^3P_2$  and  $2^3S_1 \rightarrow 2^3P_0$  in  $^{11}\text{B}^{3+}$  with 282 nm light, a diode-pumped frequency-doubled Nd:Yag continuous wave (cw) laser (Millennia 20 eV, Spectra Physics) was used to pump a tunable ring-cavity dye laser (Matisse DS 2, Sirah) with about 5 W. The dye solution was Rhodamine 110 dissolved in ethylene-glycol with a concentration of 1.93 g/L. Approximately 400 mW of fundamental power produced by the dye laser was fed into a second-harmonic generation (SHG) unit (Wavetrain 2, Spectra Physics), generating an output power of approximately 30 mW at 282 nm. The beam is directed through a pinhole to obtain a pure TEM<sub>00</sub> spatial mode and is then transported to the ODR. We used a commercial beam stabilization system from MRC systems consisting of two piezo-actuated mirrors (PAM) and position-sensitive detectors (PSD) for spacial beam stabilization and to establish a reproducible superposition of laser and ion beam in vertical direction through the SPECTRAP magnet and the ODR.

Single-mode operation and short-term frequency stabilization of the tunable dye laser were achieved by a side-of-fringe lock onto the transmission signal of a reference cavity. Long-term frequency stabilization and the laser frequency scanning were realized by a software-controlled feedback loop based on the readout of the high-precision wavelength-meter WSU10 (High-Finesse), which was calibrated with a frequency comb at TU Darmstadt [31].

To extract the rest-frame transition frequency from the observed laboratory-frame transition frequency, the relativistic Doppler effect has to be taken into account. The laboratory-frame transition frequency  $\nu_{\text{lab}}$  is shifted with respect to the rest-frame transition frequency  $\nu_0$  in collinear or anticollinear laser spectroscopy according to

$$\nu_{\text{lab}} = \nu_0 \gamma (1 \pm \beta). \quad (4)$$

Here,  $\beta = v/c$  is the ion velocity in units of the speed of light and  $\gamma = 1/\sqrt{1-\beta^2}$  is the usual relativistic time dilation factor. Thus, the exact ion velocity is required to determine the rest-frame transition frequency. This can be avoided if spectra in collinear and anticollinear direction are recorded with ions of the same velocity (quasi-)simultaneously. This leads to an expression for the rest-frame transition frequency of

$$\nu_0 = \sqrt{\nu_{\text{col}} \nu_{\text{acol}}} \tag{5}$$

Collinear spectra were recorded by retro-reflecting the beam with a mirror above the upper viewport back into the ODR and tuning the laser to the blue-shifted resonance wavelength for collinear excitation. Collinear spectra, therefore, have a significantly deteriorated signal-to-background and signal-to-noise (S/N) ratio, since the laser beam passes the ODR twice but only the collinear beam produces a signal.

### 3. Results

All spectra were taken by recording the optical resonance fluorescence as a function of the laser frequency which was tuned across the resonance line. Collinear spectra could only be recorded for the  $2^3S_1 (F = 5/2) \rightarrow 2^3P_2 (F = 7/2)$  of the  $^{11}\text{B}^{3+}$  hyperfine-multiplet, due to the reduced S/N ratio in this geometry. This line therefore served as a reference line and its transition frequency was measured in collinear–anticollinear geometry. All other transitions, indicated by dashed lines in Figure 3, were investigated only in anticollinear geometry. Spectra of the reference line obtained in anticollinear and collinear geometry are depicted in Figure 4a,b, respectively.

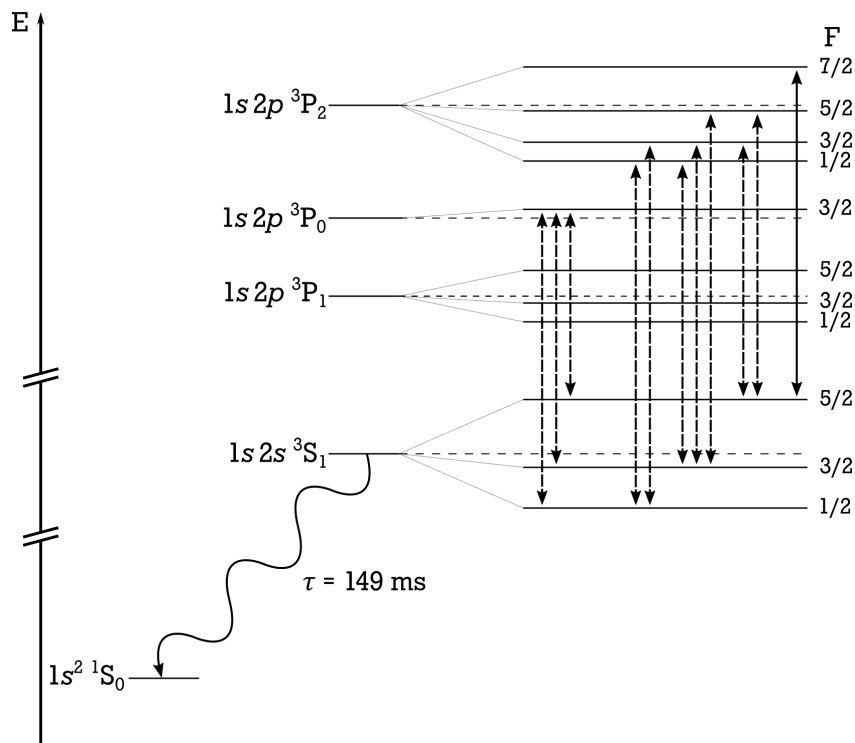


**Figure 3.** Level scheme of  $^{11}\text{B}^{3+}$ . All transitions, which were measured during the measurement campaign, are indicated by straight arrows: The strongest hyperfine transition that was used as reference line is the solid line, while all others are indicated by the dashed lines. The M1-transition from the metastable  $2s2p\ ^3S_1$  to the ground state  $1s^2\ ^1S_0$  is depicted with its lifetime  $\tau = 149\text{ ms}$  taken from [32].

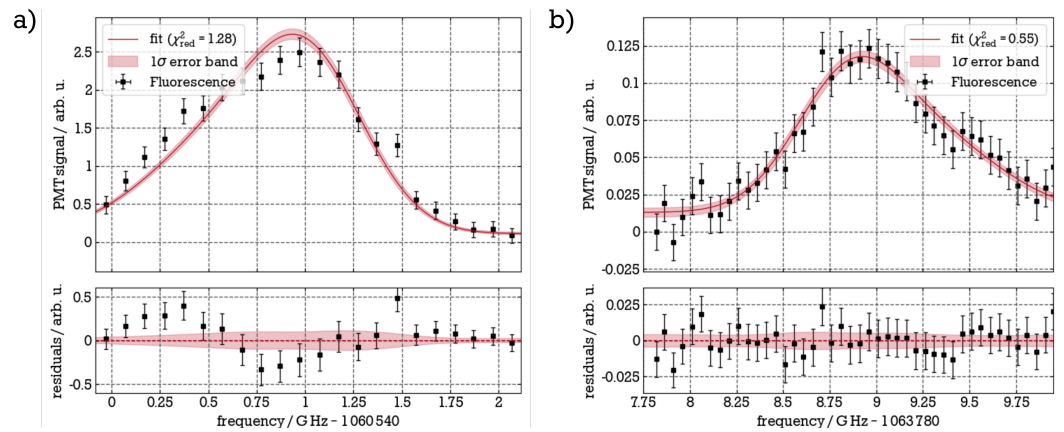


**Figure 4.** Anticollinear and collinear measurements of the reference transition  $2^3S_1 (F = 5/2) \rightarrow 2^3P_2 (F = 7/2)$  evaluated with the asymmetric Gaussian fit-model. In the collinear setup (b), the laser passed the optical detection region twice, but only one way contributes to the signal. Hence, the signal-to-noise ratio is worse compared to the anticollinear geometry (a). The anticollinear measurement was performed subsequently to the collinear measurement. Only the mirror on top of the vertical SPECTRAP beamline was removed. The difference between the main and the satellite peak in the asymmetric Gaussian profile was fixed, but with opposite sign for the two geometries.

The clear asymmetry of the spectra are most probably caused by the switching process of the confinement electrode during the ejection process of the ions. Ions, which are in the fringe field of the capture electrode while the potential is decreased, do not experience the total acceleration potential of the trap’s central drift electrode. This translates into lower (higher) laboratory frame transition frequencies in anticollinear (collinear) geometry, respectively, which is evident in the signal tails of Figure 4. One strength of the collinear–anticollinear approach is that many systematic shifts such as this asymmetry largely cancel in Equation (5) when they lead to opposite frequency shifts in the spectra taken with the copropagating and the counterpropagating laser beam [33,34]. In order to estimate the remaining systematic uncertainty, we varied the length and time period of photon acceptance, which leads to a variation of the signal asymmetry. The obtained resonance signals were also fitted with various lineshapes, among them symmetric (Gaussian, Voigt, Lorentzian) as well as asymmetric profiles (Fano–Voigt and asymmetric Gaussian, i.e., a Gaussian with a secondary peak at a varying offset). Analysis of all collinear–anticollinear measurements for three different time intervals and the five fitting functions resulted in a total standard deviation of only 15 MHz. Additional uncertainties arise from a possible misalignment between the two laser and the ion beams, which is estimated to be 17 MHz, and the wavemeter uncertainty that was conservatively estimated as the maximum deviation observed in the calibration reported in [31] (20 MHz). Variations of the ion arrival time, the EBIT voltages, and space charge of the ion beam between collinear and anticollinear measurement were also taken into account and contribute to the total uncertainty of approximately 60 MHz ( $1\sigma$ ) at the current stage of analysis, where all systematical and statistical contributions are added in quadrature. The final rest-frame transition frequency from all measurements is, thus, obtained as

$$\nu_{0,\text{ref}} = 1\,062\,163.69 (6) \text{ GHz.} \tag{6}$$

All other hyperfine lines were measured relative to the reference transition in anti-collinear geometry. For these cases, the following procedure was used: the temporally closest measurement of the reference transition  $\nu_{1,\text{ref}}$  in combination with the rest-frame transition frequency  $\nu_{0,\text{ref}}$  from Equation (6) was used to eliminate the ion velocity in

Equation (4). Hence, the measured laboratory frequency  $\nu_{1,x}$  of a hyperfine transition  $x$  was transformed into the rest-frame according to

$$\nu_{0,x} = \frac{\nu_{0,\text{ref}}}{\nu_{1,\text{ref}}} \cdot \nu_{1,x}. \tag{7}$$

In this case, systematic uncertainties cancel to a much less degree, and the combined uncertainty is of the order of 200 MHz, almost four times as large as for the reference line. The full hyperfine spectrum of the  $2^3S_1 \rightarrow 2^3P_2$  and  $2^3S_1 \rightarrow 2^3P_0$  transitions, combined from the measurements of the individual lines, is depicted in Figure 5.

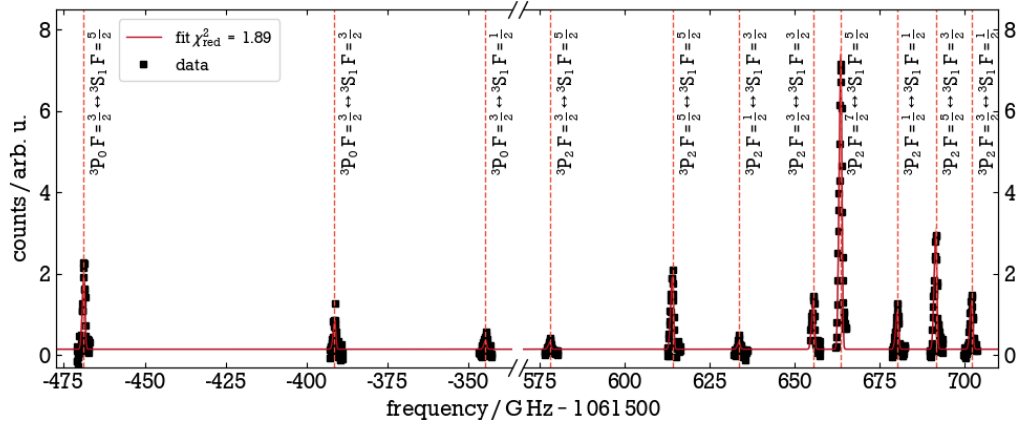


**Figure 5.** Complete hyperfine spectrum of the  $2^3S_1 \rightarrow 2^3P_0$  and  $2^3S_1 \rightarrow 2^3P_2$  fine-structure transitions including the fit of the hyperfine transitions, including hyperfine-induced fine-structure mixing, as discussed in the text. The individual transitions are indicated at the resonances.

#### 4. Discussion

Due to the dense-lying  $2^3P_J$  fine-structure levels, hyperfine-induced mixing leads to significant changes of the resulting energy levels. The most recent calculations of the mixing amplitudes in He-like systems were presented by Johnson et al. [35]. In order to extract the fine-structure transitions from the experimental data, a fitting routine was developed using the transition frequencies of the respective fine-structure transitions and the magnetic and electric hyperfine constants  $A$  and  $B$  of the  $^3S_1$  state as free parameters. Following the definitions detailed in [35], the hyperfine transitions were calculated by diagonalization of the mixing matrix, for which the matrix elements and the nuclear  $g$ -factor of  $^{11}\text{B}^{3+}$  were taken from [35,36], respectively. Since no hyperfine transitions of the  $2^3S_1 \rightarrow 2^3P_1$  multiplet were measured, its corresponding fine-structure transition frequency parameter was fixed to the theoretical value provided by Yerokhin et al. [37]. The fine-structure splitting obtained by this procedure is given in Table 1 and is compared to former experimental and theoretical values.

**Table 1.** Preliminary result for the  $2^3P_2 - 2^3P_0$  fine-structure splitting in  $^{11}\text{B}^{3+}$ . Numbers are given in  $\text{cm}^{-1}$ , and  $1\sigma$  uncertainty is indicated in parentheses if available. The final analysis is expected to provide an even more accurate value.

	$2^3P_2 - 2^3P_0$	Ref.
Schiff, 1973	36.416	[38]
Drake, 1988	36.32 (11)	[39]
Dinn�en (exp.), 1991	36.457 (9)	[24]
Chen, 1993	36.450 (40)	[40]
Yerokhin, 2010	36.460 (20)	[37]
Yerokhin, 2022	36.467 (5)	[18]
This work (exp.)	36.462 (10)	

The results of our analysis are in excellent agreement with the former experimental determination in [24] as well as the theoretical prediction by Yerokhin and coworkers [18,37]. It should be emphasized that the discrepancies with the theoretical predictions by Drake et al. [39] were ascribed to higher-order effects in the  $m\alpha$  expansion lacking in the NR-QED approach [24]. This was partially supported by the relativistic configuration interaction (CI) calculations by Chen et al. [40], where relativistic effects were naturally included and led to a better agreement. Finally, the treatment of higher orders in the NR-QED approach up to  $m\alpha^6$  substantiated this assumption. Even though only a moderate improvement in accuracy was achieved, our experimental value is in good agreement with the previous one and paves the way towards high-precision laser spectroscopy on He-like systems at the COALA beamline. The following aspects are important for future work: First, it was unambiguously demonstrated that the metastable triplet  $2^3S_1$  state is sufficiently populated for collinear laser spectroscopy during the production of  $^{11}\text{B}^{3+}$  ions in an EBIT. Second, experimental conditions at the EBIT should be improved to obtain a more symmetric lineshape and—if possible—to reduce the linewidth. One possibility could be the so-called leakage mode of the EBIT, where the potential at the exit electrode is lowered such that some ions can escape from the trap and are continuously accelerated into the beamline. The investigation of this mode was not possible under the conditions at the HITRAP beamline but are currently ongoing with a dedicated electron beam ion source (EBIS) at COALA, where, especially, a much lower background rate is achieved. Furthermore, a careful analysis of systematic effects on the extracted fine-structure transition frequencies due to uncertainties in the theoretical predictions for the mixing amplitudes is missing and must be conducted before the all-optical approach can be applied to those isotopes.

## 5. Conclusions

Within this pilot experiment, we successfully demonstrated that the metastable  $2^3S_1$  state in  $^{11}\text{B}^{3+}$  ions is sufficiently populated in an ion beam extracted from an electron beam ion trap (EBIT) to perform collinear laser spectroscopy with resonance fluorescence detection. Even under the improvised conditions at the HITRAP low-energy beamline at the GSI Helmholtz Center, it was possible to determine the fine-structure transition frequencies for the  $2^3S_1 \rightarrow 2^3P_{0,2}$  transitions and to extract the fine-structure splitting  $^3P_2 - ^3P_0$ , which was compared to former results. Due to the dense-lying fine-structure levels, a mixing of hyperfine states leads to shifted energy-levels, which causes additional unrated uncertainties for the determination of fine-structure transition frequencies. Hence, an ideal candidate to demonstrate the feasibility of the all-optical approach is carbon, where the most abundant even isotope  $^{12}\text{C}$  does not exhibit a hyperfine structure. Additionally, the odd isotope  $^{13}\text{C}$  can be used to characterize uncertainties arising from the hyperfine mixing. These are the first steps planned at the COALA beamline.

**Author Contributions:** K.M., A.B., P.I., B.M., V.H. and Z.A. conceptualized the experiment. W.N. and C.W. were responsible for project administration and funding acquisition. K.M., R.S. and P.I. prepared and installed the laser system. A.B., V.H. and C.W. designed and implemented the optical detection region. K.M. developed the DAQ. M.H., S.R. and K.K. prepared and operated the EBIT. K.M., A.B., M.H., R.S. and S.R. conducted the experiment. K.M. and A.B. analyzed the data. K.M. and W.N. cowrote the first draft of the manuscript. The manuscript was then read, improved, and finally approved by all authors. All authors have read and agreed to the published version of the manuscript.

**Funding:** We acknowledge support from the BMBF under contract numbers 05P19RDFAA, 05P21RDEA1, and 05P19PMFA1, and from the Deutsche Forschungsgemeinschaft (DFG, German Research Foundation)—Project-Id 279384907—SFB 1245, and the Open Access Publishing Fund of Technical University of Darmstadt.

**Data Availability Statement:** Data are available from the corresponding author on reasonable request.

**Conflicts of Interest:** The authors declare no conflict of interest.

## References

1. Blaum, K.; Dilling, J.; Nörtershäuser, W. Precision atomic physics techniques for nuclear physics with radioactive beams. *Phys. Scr.* **2013**, *T152*, 014017. [[CrossRef](#)]
2. Campbell, P.; Moore, I.D.; Pearson, M.R. Laser spectroscopy for nuclear structure physics. *Prog. Part. Nucl. Phys.* **2016**, *86*, 127–180. [[CrossRef](#)]
3. Lu, Z.T.; Mueller, P.; Drake, G.W.; Nörtershäuser, W.; Pieper, S.C.; Yan, Z.C. Colloquium: Laser probing of neutron-rich nuclei in light atoms. *Rev. Mod. Phys.* **2013**, *85*, 1383–1400. [[CrossRef](#)]
4. Maaß, B.; Hüther, T.; König, K.; Krämer, J.; Krause, J.; Lovato, A.; Müller, P.; Pachucki, K.; Puchalski, M.; Roth, R.; et al. Nuclear Charge Radii of  $^{10,11}\text{B}$ . *Phys. Rev. Lett.* **2019**, *122*, 1–6. [[CrossRef](#)] [[PubMed](#)]
5. Stovall, T.; Goldemberg, J.; Isabelle, D.B. Coulomb form factors of  $^{10}\text{B}$  and  $^{11}\text{B}$ . *Nucl. Phys.* **1966**, *86*, 225–240. [[CrossRef](#)]
6. Schaller, L.A.; Schellenberg, L.; Ruetschi, A.; Schneuwly, H. Nuclear charge radii from muonic X-ray transitions in beryllium, boron, carbon and nitrogen. *Nucl. Phys. A* **1980**, *343*, 333–346. [[CrossRef](#)]
7. Maaß, B.; Müller, P.; Nörtershäuser, W.; Clark, J.; Gorges, C.; Kaufmann, S.; König, K.; Krämer, J.; Levand, A.; Orford, R.; et al. Towards laser spectroscopy of the proton-halo candidate boron-8. *Hyperfine Interact.* **2017**, *238*, 25. [[CrossRef](#)]
8. Antognini, A.; Bacca, S.; Fleischmann, A.; Gastaldo, L.; Hagelstein, F.; Indelicato, P.; Knecht, A.; Lensky, V.; Ohayon, B.; Pascallusa, V.; et al. Muonic-Atom Spectroscopy and Impact on Nuclear Structure and Precision QED Theory. *arXiv* **2022**, arXiv:2210.16929.
9. Udem, T.; Huber, A.; Gross, B.; Reichert, J.; Prevedelli, M.; Weitz, M.; Hänsch, T.W. Phase-Coherent Measurement of the Hydrogen 1S–2S Transition Frequency with an Optical Frequency Interval Divider Chain. *Phys. Rev. Lett.* **1997**, *79*, 2646–2649. [[CrossRef](#)]
10. Beyer, A.; Maisenbacher, L.; Matveev, A.; Pohl, R.; Khabarova, K.; Grinin, A.; Lamour, T.; Yost, D.C.; Hänsch, T.W.; Kolachevsky, N.; et al. The Rydberg constant and proton size from atomic hydrogen. *Science* **2017**, *358*, 79–85. [[CrossRef](#)]
11. Fleurbaey, H.; Galtier, S.; Thomas, S.; Bonnaud, M.; Julien, L.; Biraben, F.; Nez, F.; Abgrall, M.; Guéna, J. New Measurement of the 1S – 3S Transition Frequency of Hydrogen: Contribution to the Proton Charge Radius Puzzle. *Phys. Rev. Lett.* **2018**, *120*, 183001. [[CrossRef](#)] [[PubMed](#)]
12. Pohl, R.; Antognini, A.; Nez, F.; Amaro, F.D.; Biraben, F.; Cardoso, J.M.; Covita, D.S.; Dax, A.; Dhawan, S.; Fernandes, L.M.; et al. The size of the proton. *Nature* **2010**, *466*, 213–216. [[CrossRef](#)] [[PubMed](#)]
13. Pohl, R.; Nez, F.; Fernandes, L.M.P.; Amaro, F.D.; Biraben, F.; Cardoso, J.M.R.; Covita, D.S.; Dax, A.; Dhawan, S.; Diepold, M.; et al. Laser spectroscopy of muonic deuterium. *Science* **2016**, *353*, 669–673. [[CrossRef](#)] [[PubMed](#)]
14. Krauth, J.J.; Schuhmann, K.; Ahmed, M.A.; Amaro, F.D.; Amaro, P.; Biraben, F.; Chen, T.I.; Covita, D.S.; Dax, A.J.; Diepold, M.; et al. Measuring the  $\alpha$ -particle charge radius with muonic helium-4 ions. *Nature* **2021**, *589*, 527–531. [[CrossRef](#)] [[PubMed](#)]
15. Karr, J.P.; Marchand, D.; Voutier, E. The proton size. *Nat. Rev. Phys.* **2020**, *2*, 601–614. [[CrossRef](#)]
16. Yerokhin, V.A.; Patkóš, V.c.č.; Pachucki, K. Relativistic corrections to the Bethe logarithm for the  $2\ ^3\text{S}$  and  $2\ ^3\text{P}$  states of He. *Phys. Rev. A* **2018**, *98*, 32503. [[CrossRef](#)]
17. Patkóš, V.; Yerokhin, V.A.; Pachucki, K. Nonradiative  $\alpha^7 m$  QED effects in Lamb shift of helium triplet states. *Phys. Rev. A* **2021**, *103*, 042809. [[CrossRef](#)]
18. Yerokhin, V.A.; Patkóš, V.; Pachucki, K. QED calculations of energy levels of heliumlike ions with  $5 \leq Z \leq 30$ . *Phys. Rev. A* **2022**, *106*. [[CrossRef](#)]
19. Anton, K.R.; Kaufman, S.L.; Klempt, W.; Moruzzi, G.; Neugart, R.; Otten, E.W.; Schinzler, B. Collinear Laser Spectroscopy on Fast Atomic Beams. *Phys. Rev. Lett.* **1978**, *40*, 642–645. [[CrossRef](#)]
20. Imgram, P.; König, K.; Krämer, J.; Ratajczyk, T.; Maaß, B.; Müller, P.; Sommer, F.; Nörtershäuser, W. High-precision collinear laser spectroscopy at the Collinear Apparatus for Laser Spectroscopy and Applied Physics (COALA). *Hyperfine Interact.* **2020**, *241*, 48. [[CrossRef](#)]
21. Müller, P.; König, K.; Imgram, P.; Krämer, J.; Nörtershäuser, W. Collinear laser spectroscopy of  $\text{Ca}^+$ : Solving the field-shift puzzle of the  $4s\ ^2\text{S}_{1/2} \rightarrow 4p\ ^2\text{P}_{1/2,3/2}$  transitions. *Phys. Rev. Res.* **2020**, *2*, 1–13. [[CrossRef](#)]
22. Neugart, R.; Billowes, J.; Bissell, M.L.; Blaum, K.; Cheal, B.; Flanagan, K.T.; Neyens, G.; Nörtershäuser, W.; Yordanov, D.T. Collinear laser spectroscopy at ISOLDE: new methods and highlights. *J. Phys. G* **2017**, *44*, 064002. [[CrossRef](#)]
23. König, K.; Krämer, J.; Geppert, C.; Imgram, P.; Maaß, B.; Ratajczyk, T.; Nörtershäuser, W. A new Collinear Apparatus for Laser Spectroscopy and Applied Science (COALA). *Rev. Sci. Instrum.* **2020**, *91*, 081301. [[CrossRef](#)]
24. Dinneen, T.P.; Berrah-Mansour, N.; Berry, H.G.; Young, L.; Pardo, R.C. Precision measurements of relativistic and QED effects in helium-like boron. *Phys. Rev. Lett.* **1991**, *66*, 2859–2862. [[CrossRef](#)] [[PubMed](#)]
25. Sokolov, A.; Herfurth, F.; Kester, O.; Stoehlker, T.; Thorn, A.; Vorobjev, G.; Zschornack, G. SPARC EBIT—A charge breeder for the HITRAP project. *J. Instrum.* **2010**, *5*, C11001. [[CrossRef](#)]
26. Andelkovic, Z.; Herfurth, F.; Kotovskiy, N.; König, K.; Maaß, B.; Murböck, T.; Neidherr, D.; Schmidt, S.; Steinmann, J.; Vogel, M.; et al. Beamline for low-energy transport of highly charged ions at HITRAP. *Nucl. Instrum. Methods Phys. Res. Sect. A* **2015**, *795*, 109–114. [[CrossRef](#)]

27. Andelkovic, Z.; Cazan, R.; Nörtershäuser, W.; Bharadia, S.; Segal, D.M.; Thompson, R.C.; Jöhren, R.; Vollbrecht, J.; Hannen, V.; Vogel, M. Laser cooling of externally produced Mg ions in a Penning trap for sympathetic cooling of highly charged ions. *Phys. Rev. A* **2013**, *87*, 033423. [[CrossRef](#)]
28. Buß, A. Development of Fluorescence Detectors for Laser Spectroscopy Experiments at GSI/FAIR, and Measurement of Hyperfine Transitions between the  $2^3P$  and  $2^3S$  States in Helium-like Boron. Ph.D. Thesis, WWU Münster, Münster, Germany, 2022.
29. Mohr, K.T. First laser spectroscopy of  $Mg^+$  at CRYRING@ESR and He-Like Boron at HITRAP. Ph.D. Thesis, TU Darmstadt, Darmstadt, Germany, 2022. [[CrossRef](#)]
30. Malbrunot-Ettenauer, S.; Kaufmann, S.; Bacca, S.; Barbieri, C.; Billowes, J.; Bissell, M.L.; Blaum, K.; Cheal, B.; Duguet, T.; Ruiz, R.F.G.; et al. Nuclear Charge Radii of the Nickel Isotopes  $^{58-68.70}Ni$ . *Phys. Rev. Lett.* **2022**, *128*, 022502. [[CrossRef](#)]
31. König, K.; Imgram, P.; Krämer, J.; Maaß, B.; Mohr, K.; Ratajczyk, T.; Sommer, F.; Nörtershäuser, W. On the performance of wavelength meters: Part 2—Frequency-comb based characterization for more accurate absolute wavelength determinations. *Appl. Phys. B* **2020**, *126*, 86. [[CrossRef](#)]
32. Drake, G.W.F. Theory of Relativistic Magnetic Dipole Transitions: Lifetime of the Metastable  $2^3S$  State of the Heliumlike Ions. *Phys. Rev. A* **1971**, *3*, 908–915. [[CrossRef](#)]
33. Krieger, A.; Nörtershäuser, W.; Geppert, C.; Blaum, K.; Bissell, M.L.; Frömmgen, N.; Hammen, M.; Kreim, K.; Kowalska, M.; Krämer, J.; et al. Frequency-comb referenced collinear laser spectroscopy of  $Be^+$  for nuclear structure investigations and many-body QED tests. *Appl. Phys. B* **2017**, *123*, 15. [[CrossRef](#)]
34. Renth, L.; Imgram, P.; Krämer, J.; König, K.; Lellinger, T.; Maaß, B.; Müller, P.; Ratajczyk, T.; Nörtershäuser, W. First experiments with a laser ablation source at the COALA setup. *Hyperfine Interact.* **2020**, *241*, 56. [[CrossRef](#)]
35. Johnson, W.R.; Cheng, K.T.; Plante, D.R. Hyperfine structure of  $2^3P$  levels of heliumlike ions. *Phys. Rev. A* **1997**, *55*, 2728–2742. [[CrossRef](#)]
36. Stone, N.J. Table of nuclear magnetic dipole and electric quadrupole moments. *At. Data Nucl. Data Tables* **2005**, *90*, 75–176. [[CrossRef](#)]
37. Yerokhin, V.A.; Pachucki, K. Theoretical energies of low-lying states of light helium-like ions. *Phys. Rev. A* **2010**, *81*, 022507. [[CrossRef](#)]
38. Schiff, B.; Accad, Y.; Pekeris, C.L. Correction to the  $n^3P_1$  Levels of the Helium Isoelectronic Sequence Owing to Mixing with the  $n^1P_1$  State. *Phys. Rev. A* **1973**, *8*, 2272–2273. [[CrossRef](#)]
39. Drake, G.W. Theoretical energies for the  $n = 1$  and  $2$  states of the helium isoelectronic sequence up to  $Z = 100$ . *Can. J. Phys.* **1988**, *66*, 586–611. [[CrossRef](#)]
40. Chen, M.H.; Cheng, K.T.; Johnson, W.R. Relativistic configuration-interaction calculations of  $n = 2$  triplet states of heliumlike ions. *Phys. Rev. A* **1993**, *47*, 3692–3703. [[CrossRef](#)]

**Disclaimer/Publisher’s Note:** The statements, opinions and data contained in all publications are solely those of the individual author(s) and contributor(s) and not of MDPI and/or the editor(s). MDPI and/or the editor(s) disclaim responsibility for any injury to people or property resulting from any ideas, methods, instructions or products referred to in the content.